

# Detection of Martian Dust Storms Using Mask-Regional Convolutional Neural Networks

Rasha Alshehhi (✉ [ra130@nyu.edu](mailto:ra130@nyu.edu))

NYU Abu Dhabi: New York University - Abu Dhabi Campus

Claus Gebhardt

UAE University: United Arab Emirates University

---

## Methodology

**Keywords:** Mars, dust storm, Mask Regional Convolutional Neural Networks, average precision score

**Posted Date:** August 2nd, 2021

**DOI:** <https://doi.org/10.21203/rs.3.rs-729496/v1>

**License:** © ⓘ This work is licensed under a Creative Commons Attribution 4.0 International License.

[Read Full License](#)

---

**Version of Record:** A version of this preprint was published at Progress in Earth and Planetary Science on January 9th, 2022. See the published version at <https://doi.org/10.1186/s40645-021-00464-1>.

## RESEARCH

# Detection of Martian dust storms using mask-regional convolutional neural networks

Rasha Alshehhi<sup>1\*</sup> and Claus Gebhardt<sup>2</sup>

\*Correspondence: [ra130@nyu.edu](mailto:ra130@nyu.edu)

<sup>1</sup>Center for Space Science, New York University, Abu Dhabi United Arab Emirate

Full list of author information is available at the end of the article

## Abstract

Martian dust plays a crucial role in the meteorology and climate of the Martian atmosphere. It heats the atmosphere, enhances the atmospheric general circulation, and affects spacecraft instruments and operations. Compliant with that, studying dust is also essential for future human exploration. In this work, we present a method for the deep-learning-based detection of the areal extent of dust storms in Mars satellite imagery. We use a mask regional convolutional neural network (R-CNN), consisting of a regional-proposal network (RPN) and a mask network. We apply the detection method to Mars Daily Global Maps (MDGMs) of the Mars Global Surveyor (MGS) Mars Orbiter Camera (MOC). We use center coordinates of dust storms from the eight-year Mars Dust Activity Database (MDAD) as ground-truth to train and validate the method. The performance of the regional network is evaluated by the average precision score with 50% overlap ( $mAP_{50}$ ), which is around 62.1%.

## Keywords

Mars; dust storm; Mask Regional Convolutional Neural Networks; average precision score

## 1 Introduction

The Martian dust cycle is of fundamental importance to the meteorology and climate of the Martian atmosphere (e.g., [Hab17](#); [Kas16](#); [Mon15](#)). Atmospheric dust absorbs and scatters solar and infrared radiation. It thus increases the atmospheric temperature and enhances the atmospheric general circulation (e.g. [Geb20](#); [New15](#)). Moreover, dust storms are a very common phenomenon on Mars. Every few Martian years, on average, global dust storm events occur. Hence, the Mars dust cycle has implications for spacecraft engineering parameters, the entry-descent-landing (EDL) operation of spacecraft, the energy production by the solar panels of Mars rovers/landers, etc. Also, it is an essential concern for future human exploration of Mars.

Martian dust storms are evident as frontal features ([Wan15](#)), dust storm texture/convective features ([Guz15](#)), and dust clouds ([Can19](#)). Based on the definition of ([Can01](#)), regional dust storms differ from local dust storms by having an area of  $\geq 1.6 \times 10^6 \text{ km}^2$  and a duration of more than two days. Global dust storm events (GDEs) or Planet-encircling dust storms start as local/regional dust storms and engulf the entire planet ([For17](#)). Still, dust lifting takes place at the regional scale and GDEs have several active dust lifting centers. GDEs have a duration of up to a few months and occur, by average, each few Martian Years ([Zur93](#)). While there

20 may be local and regional dust storms at any time of the Martian year, GDEs oc-  
21 cur only during the second half of the Martian year ( $L_s = 180^\circ\text{--}360^\circ$ ). The latter is  
22 known as the dust storm season and coincides with the Mars southern hemisphere  
23 spring and summer. A yearly repeatable phenomenon is multiple local dust storms  
24 at the northern/southern Mars polar edge in the respective hemispheric fall to the  
25 spring season, known as polar cap edge storms. By contrast, dust devils are another  
26 phenomenon and have a diameter of less than 1 km and a duration of fewer than  
27 10 minutes (For17).

28 A comprehensive dust climatology was detailed in (Mon15). The basis for that are  
29 data on the column dust optical depth from the satellite instruments MCS/MRO  
30 (Mars Climate Sounder/MARS Reconnaissance Orbiter), THEMIS/MO (Thermal  
31 Emission Imaging System/Mars Odyssey), and TES/MGS (Thermal Emission Spec-  
32 trometer/Mars Global Surveyor). The latter operate at different wavelength ranges,  
33 measurement geometries, and spatial and temporal coverage. This dust climatol-  
34 ogy is made publicly available via the Mars Climate Database (MCD) [1], to-  
35 gether with many other parameters of the Mars atmosphere and surface. It has  
36 a moderate spatial resolution of few degree latitude and longitude [2] and was  
37 demonstrated to be suitable to follow the evolution of certain regional dust storms  
38 by (Mon15). Various studies identified and explored dust storms based on the  
39 visual inspection of Mars Daily Global Maps (MDGMs) from the camera sys-  
40 tem MOC/MGS (Can07; Hin12). Other studies focused on MDGMs from both  
41 MOC/MGS and MARCI/MRO (Bat21; Wan15). In this work, we perform feasibility  
42 study on a deep-learning-based approach for dust storm detection from the record  
43 of MDGMs by the Mars Orbiter Camera (MOC) (Mal10) aboard the Mars Global  
44 Surveyor (MGS), by applying convolutional neural networks (CNNs) (Sim14).

45 Recently, deep convolutional networks have made significant improvements in the  
46 accuracy of object detection. As widely known, object detection is a challenging task  
47 because it requires the accurate localization of candidate objects. In this paper, we  
48 use mask regional convolutional neural networks (R-CNNs) that jointly learn to  
49 classify dust storm candidates and refine their spatial locations. The spatial loca-  
50 tion of potential dust storm candidates (i.e., the ground-truth objects) may be to  
51 a certain degree arbitrary because dust storm boundaries are identified based on  
52 the subjective perception of individual observers and are interpolated if intersecting  
53 satellite image gaps and/or the polar night. Here we make the simplifying assump-  
54 tion that dust storms have a rectangular shape around their central coordinates.

55 The main contribution of this work can be summarized as follows:

- 56 • It is the first work on the deep-learning-based detection of Mars dust storms  
57 which is applied to several Martian-year records of MDGMs. Also, it uses the  
58 Mars dust storm database of Battalio and Wang (Bat21), which is one of the  
59 most recent and comprehensive of its kind, as a ground-truth.
- 60 • It uses a new architecture that consists of two networks to enhance the bound-  
61 aries of dust storm areas, although the ground-truth boundaries include a  
62 certain degree of subjectivity and arbitrariness.

---

[1]<http://www-mars.lmd.jussieu.fr/>

[2][http://www-mars.lmd.jussieu.fr/mars/dust\\_climatology/index.html](http://www-mars.lmd.jussieu.fr/mars/dust_climatology/index.html)

- It uses a dice score as mask loss function to overcome ambiguous cases at the boundary between a dust storm and non-dust-storm categories with a lower level of uncertainty between the two categories.

The outline of this paper is the following. Section 2 describes the previous work related to automated dust storm detection and the latest R-CNN techniques. In Section 3, we explain the observation-based dataset and ground-truth we used. In Section 4, we illustrate the methodology to detect dust storms on the Martian surface. We discuss the performance of our method in Section 5. In Section 6, we summarize the main findings and provide an outlook for the future.

## 2 Related work

### 2.1 Detection of Martian dust storms

Maeda et al. (Mae15) proposed an automatic method to detect dust storms. Their method is based on selected features using minimal redundancy maximal relevance algorithm and classification using Support Vector Machine (SVM). It successfully detects around 80% of dust storms, but it did not define the locations of dust storms. Gichu and Ogohara (Gic19) suggested a segmentation method to classify Martian images into either dust areas or cloud areas. They used principle component analysis (PCA) and supervised multi-layer perceptron (MLP) neural networks based on subjective ground-truth images. They only focused on the regions (patches) with a high frequency of dust storms revealed by Guzewich et al. (Guz15) and Kulowski et al. (Kul17). In this work, we concentrate on complete Martian images.

### 2.2 Regional convolutional neural networks (R-CNNs)

The R-CNNs are used to predict object's position and objectness scores at each position. Girshick et. al. (Gir13) proposed the first R-CNN by generating CNN features of each object proposal and applying the SVM to classify proposals. The fast R-CNN is a new version of the previous R-CNN. It trains the very deep VGG16 network faster by  $9\times$  and  $213\times$  at train time and test time, respectively. Ren et. al. (Ren16) introduced a regional proposal network (RPN) that shares full-image convolutional features and merges with the detection fast R-CNN. The PRN works as an attention mechanism telling the fast-RCN where to look. He et al. (He17) integrated fast R-CNN with segmentation to generate a high-quality mask for each object instance in the image (mask R-CNN). Cheng at al. (Che20) presents a boundary-preserving mask R-CNN that explicitly exploits object boundary to improve localization accuracy. In this work, we use mask R-CNN to determine the whole area of dust storms in Martian images.

## 3 Data

As ground-truth images, we use the Mars Dust Activity Database (MDAD) (Bat21). It is a dust storm database compiled from eight Martian years (MY) of Mars Daily Global Maps (MDGMs), which means from MY 24, Ls  $150^\circ$  (1999) to MY 32, Ls  $171^\circ$  (2014). The MDAD comprises 14,974 dust storm instances, which are, by definition, enclosed dust storm regions on a single sol (Martian day). The dust storm instances are combined into 7,927 dust storm members. These are subdivided further into a total of 228 dust storm sequences (125 originated in the northern

106 hemisphere and 103 in the southern hemisphere). Dust storm members are multi-  
107 sol dust storm instances that can be tracked from one sol to the next. Dust storm  
108 sequences are one or more dust storm members following a coherent trajectory and  
109 having a lifetime of at least three sols.

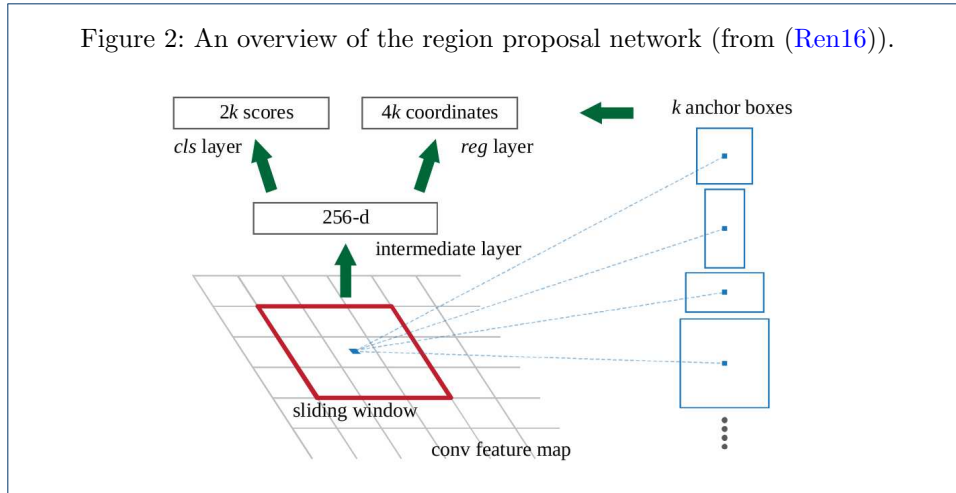
110 Unorganized dust storm instances are equivalent to dust storm members having  
111 just one constituent. The latter are found mostly along with the polar ice cap  
112 edges in the northern and southern hemispheres around their respective fall and  
113 winter seasons (i.e., polar cap edge storms). These unorganized instances do not  
114 change much between different Martian years in terms of latitude, timing, and  
115 number. By contrast, the most dominant sources of interannual variability are the  
116 global dust storm events at around Ls  $185^{\circ}$ – $210^{\circ}$  in MY 25 and Ls  $265^{\circ}$ – $290^{\circ}$  in  
117 MY 28. The Mars Dust Activity Database can be found at [https://doi.org/10.](https://doi.org/10.7910/DVN/F8R2JX)  
118 [7910/DVN/F8R2JX](https://doi.org/10.7910/DVN/F8R2JX). It includes the center coordinates (longitude and latitude) and  
119 area (in  $km^2$ ) of individual dust storm instances. We use the center coordinates of  
120 each such dust storm instance but, as a simplifying assumption, consider rectangle  
121 areas around the center coordinates. The MDAD also includes confidence levels  
122 (CL) of 100, 75, and 50, which are assigned to each dust storm instance based on  
123 visual inspection. They rate the accuracy of dust storm boundaries with the highest  
124 confidence level of 100 and the lowest confidence level of 25.  $CL = 100$  means the  
125 entire perimeter of the dust storm instance is distinct against the background so that  
126 the dust storm edge has an error on the order of a few pixels only (which is equivalent  
127 with approximately  $0.5^{\circ}$ ).  $CL = 25$  shows rather nebulous boundaries that cannot  
128 be exactly discerned from the background within few degrees of latitude/longitude.  
129 The CL is also used to determine how distinct a dust storm instance is from the  
130 background atmospheric opacity. Only dust storm instances with  $CL = 100, 75, 50$   
131 are listed in the MDAD.

132 In the following, we include all Mars Daily Global Maps (MDGMs) based on  
133 MOC/MGS, from MY 24, Ls  $150^{\circ}$  (1999) to MY 28, Ls  $121^{\circ}$  (2006), as obtained  
134 from <https://doi.org/10.7910/DVN/WWRT1V>. We consider the non-polar versions  
135 of these MDGMs, which cover latitudes from  $60^{\circ}$ N– $60^{\circ}$ S and longitudes from  $180^{\circ}$ E–  
136  $180^{\circ}$ W and have simple cylindrical map projection. The MDGMs have a resolution  
137 of 7.5 km per pixel with  $0.1^{\circ}$  longitude by  $0.1^{\circ}$  latitude. They are available as RGB  
138 images. Details on the MDGM production process can be found in (Wan02). Each  
139 MDGM is based on 13 wide-angle global map swath images of the Mars Global  
140 Surveyor (MGS) Mars Orbiter Camera (MOC). The latter covers the whole sun-lit  
141 planet around 2 PM local time each sol. The MDGMs consist of imagery from the  
142 two visible bands, red (575–625 nm) which is more sensitive to dust storms, and  
143 blue (400–450 nm) which is more sensitive to water ice clouds (Can01). The green  
144 component of the MDGMs is synthesized by combining 1/3 red and 2/3 blue and  
145 applying linear stretching.

## 146 4 Method

147 We use a mask regional convolutional neural network (Mask R-CNN) to estimate  
148 the spatial probabilities of each dust storm in the Martian map. The Mask R-  
149 CNN is a modified version of fast R-CNN (Gir15), but it has a new branch masker  
150 that predicts a segmentation mask on each region of interest (RoI) in pixel-to-pixel





map of each RoI in parallel to predict the class and box boundaries from the classification/regression network. The FPN is a top-down architecture to build a pyramid from a single scale input and extract RoI features from different levels of the feature pyramid according to scale. The input of this network is  $v \times v \times l$  spatial window of feature maps from the backbone network and the output is a pixel-pixel mask with  $v \times v \times c$ , where  $l$  is the number of channels in feature maps and  $c$  is the number of classes.

We use RoIAlign (He17) as a standard sampling/quantization operation to extract RoI from feature maps for both classification/regression network and segmentation mask network. In the mask network, we use RoIAlign from feature pyramid level  $\{P_2, P_3, P_4, P_5\}$ , as in (Lin17), in the first phase of the mask network ( $Masker_A$ ). While we use RoIAlign from the finest-resolution feature in the second phase of the mask network ( $Masker_B$ ). In  $Masker_A$ , the RoI feature is fed into four consecutive  $3 \times 3$  convolutions. While in  $Masker_B$ , the RoI feature is fed into two consecutive  $3 \times 3$  and fed into  $Masker_A$  after down-scaling. This process enriches mask features and obtains an accurate mask prediction with shape and edge details. Both the original and the proposed mask R-CNNs use RoIAlign as a standard sampling operation to derive feature maps for classifiers, box regressors and maskers. However, we use separate networks for both classifier and regressor after applying full-connected layers. We also use convolution layers with various convolution kernels to extract feature maps for maskers to preserve dust boundaries' pixels and provide better localization.

### 4.3 Learning and optimization

The loss function  $L$  is a combination of classification  $L_c$ , regression  $L_r$  and segmentation mask  $L_m$  losses. We use a binary cross-entropy to classify each box and a mean absolute error (MAE) to estimate four coordinates of each box. To alleviate the class-imbalance problem between positive pixels (dust) and negative pixels (non-dust), we use Dice loss (Mil16) to measure overlapping between prediction and ground-truth.

$$L(y, \tilde{y}) = \frac{1}{N} \sum_{n=0}^N L_c(y_n, \tilde{y}_n) + L_r(y_n, \tilde{y}_n) + L_m(y_n, \tilde{y}_n), \quad (1)$$

$$L_c(y_n, \tilde{y}_n) = -y_n * \log(\tilde{y}_n) + (1 - y_n) * \log(1 - \tilde{y}_n), \quad (2)$$

$$L_r(y_n, \tilde{y}_n) = \|\tilde{y}_n - y_n\|, \quad (3)$$

$$L_m(y_n, \tilde{y}_n) = \frac{2 \sum_i^I y_n(i) * \tilde{y}_n(i)}{\sum_i^I y_n(i) + \sum_i^I \tilde{y}_n(i)}, \quad (4)$$

202 where  $N$  and  $I$  are number of anchor in each images and number of pixels of each  
 203 anchor, respectively.  $y$  and  $\tilde{y}$  are the ground-truth and the predicted probability of  
 204 each anchor  $n$ .

## 205 5 Performance

206 In this section, we present the performance of mask R-CNNs on MGS/MOC dataset  
 207 using various training strategies and compare with state-of-the-art methods.

### 208 5.1 Evaluation metrics

We assign a binary class to each RoI (anchor). We assign a positive value to RoI with the highest intersection-over-union (IoU) overlap with a ground-truth box. We assign a negative value to RoI with the lowest IoU overlap. The highest IoU ratio is 0.7 and lowest IoU ratio is 0.3. We do not use RoI that is neither positive nor negative in minimizing the objective function and mask loss  $L_m$  is defined only on positive RoIs. The IoU is defined as the area of the interaction of predicted mask  $\tilde{Y}_m = \{\tilde{y}_1^m, \dots, \tilde{y}_N^m\}$  and ground-truth mask  $Y_m = \{y_1^m, \dots, y_N^m\}$  divided by the area of the union of predicted and ground-truth masks:

$$IoU = \frac{area(Y_m \cap \tilde{Y}_m)}{area(Y_m \cup \tilde{Y}_m)}, \quad (5)$$

209 We calculate the precision ( $P = TP/TP + FP$ ) and recall ( $R = TP/TP + FN$ ) of  
 210 each image in the testing dataset, where  $TP$ ,  $FN$  and  $FP$  are the number of dust  
 211 pixels corrected classified as dust pixels, the number of dust pixels classified as non-  
 212 dust pixels and the number of non-dust pixels classified as dust pixels, respectively.  
 213 We evaluate the performance of the network based on the mean average precision  
 214 (mAP) score, where AP is an area under precision-recall curve averaging for each  
 215 class in an image. We calculate mAP at various intersection-over-union thresholds  
 216  $IoU_{th}$  (25%, 50% and 75%).

### 217 5.2 Implementation details

- 218 • Data: we use daily Martian map as an input to mask R-CNNs. We use reflected  
 219 data from red, green and blue bands from MGS/MOC maps. We prepare  
 220 the ground-truth of mask R-CNNs based on center coordinates of each dust

221 storm event in MDAD dataset (Bat21). We estimate approximate area with  
 222  $120 \times 120$  around center coordinates to draw ground-truth anchors and train  
 223 mask R-CNNs.

- 224 • Mask R-CNNs: images are resized such that their short scale is 1024 pixels. We  
 225 use five RPN anchor scales starting from  $32 \times 32$  to  $64 \times 64$ ,  $128 \times 128$ ,  $256 \times 256$   
 226 and  $512 \times 512$  on  $\{P_2, P_3, P_4, P_5, P_6\}$  layers respectively, as in (Lin17). We use  
 227 three aspect ratios  $\{1 : 2, 1 : 1, 2 : 1\}$  at each level, as in (Ren15).
- 228 • Training: we use adam optimization function. We assign the learning rate to  
 229 0.0001 which decreases by 10 every 10k iterations, weight decay to 0.001 and  
 230 momentum of 0.9, step per epoch to 1000 and validation step to 50. We train  
 231 on 1 GPU with a mini-batch size equal to 32. We train with 1 image per GPU.
- 232 • Inference: we assign the maximum number of detection instances to 100 with  
 233 confidence greater than 90%. After box prediction, we predict a binary mask  
 234 per RoI. RoI is considered positive if it has IoU with a ground-truth box of  
 235 at least 0.5.

### 236 5.3 Experimental results in different seasons

237 We use images from MY 25, Ls  $0^\circ$  to MY 27, Ls  $180^\circ$  as training dataset (1216  
 238 MDGMs). We randomly select validation images from MY 25 to MY 27 (614  
 239 MDGMs) which are not used in training dataset to validate the performance of  
 240 convolutional networks during training process to obtain lower error. We use im-  
 241 ages from MY 27, Ls  $180^\circ$  to MY 28, Ls  $121^\circ$  as a testing dataset (659 MDGMs).  
 242 Each of the datasets includes images from all four seasons: spring ( $0^\circ < Ls < 90^\circ$ ),  
 243 summer ( $90^\circ < Ls < 180^\circ$ ), fall ( $180^\circ < Ls < 270^\circ$ ) and winter ( $270^\circ < Ls < 360^\circ$ ).  
 244 The reason for using MDGMs from middle MY 27 as a testing dataset is that MY  
 245 28 only includes MDGMs from spring and summer seasons. Figure 3 and Figure 4  
 246 show ground-truth (a) and (c) and predicted regions from R-CNN (b) and (d) for  
 247 selected MDGMs of the testing dataset. In Figure 3(a), the ground-truth for MY  
 248 28, Ls  $83.04^\circ$  is given by dust storm instances at the coordinates ( $89.25^\circ W$ ,  $26.7^\circ S$ )  
 249 and ( $132.05^\circ E$ ,  $30.2^\circ N$ ). The latter have a CL=75 and CL=50, respectively, which  
 250 implies that their boundaries are not fully accurate. As follows from Figure 3(b), the  
 251 R-CNN identifies another dust storm instance close to the ground-truth dust storm  
 252 instance ( $89.25^\circ W$ ,  $26.7^\circ S$ ). However, the latter has some overlap with the true  
 253 positive dust storm instance, and may thus be considered to be not entirely false.  
 254 Figure 3(c) and 3(d) present accurate results for MY 28, Ls  $110.25^\circ$  (summer). The  
 255 ground-truth is given by dust storm instances at the coordinates ( $96.75^\circ W$ ,  $26^\circ S$ )  
 256 and ( $73.05^\circ W$ ,  $34.3^\circ S$ ) with CL=100 and CL=75 near to southern polar ice cap. The  
 257 detection accuracy is approximately 0.99 for both, i.e., high overlapping areas with  
 258 the ground-truth. Figure 4(a) and Figure 4(b) at MY 27, Ls  $222.83^\circ$ , i.e. during the  
 259 dust storm season, show that the R-CNN identifies dust storm instances in different  
 260 regions. However, it mismatches some of the center coordinates and has a certain  
 261 overlap with surrounding areas. That is the case around the ground-truth objects  
 262 at ( $148.85^\circ W$ ,  $39.5^\circ N$ ), ( $54.35^\circ W$ ,  $4.7^\circ N$ ), ( $14.65^\circ W$ ,  $46.2^\circ N$ ) with CL=50, CL=75  
 263 and CL=75, respectively. This may be at least partly due to the fact that CL=100  
 264 means the dust storms instance still has an error of few pixels, or approximately  
 265 around  $0.5^\circ$ , and CL=75 and CL=50 have an error greater than  $0.5^\circ$ , accordingly.

266 Also, it fails to distinguish the dust storm instances with  $CL=100$  and  $CL=50$  at  
 267 the coordinates  $(147.75^\circ E, 33.7^\circ N)$  and  $(46.55^\circ W, 17.9^\circ S)$  from the background. A  
 268 potential explanation for that is increased atmospheric background dustiness dur-  
 269 ing the dust storm season. Figure 4(c) and Figure 4(d) show accurate results at Ls  
 270  $305.93^\circ$  with ground-truth objects at  $(32.55^\circ W, 0.90^\circ N)$  and  $(158.55^\circ W, 36.1^\circ N)$   
 271 and  $CL = 75$ .

272 We also apply the network to images from MY 25, Ls  $0^\circ$  to MY 28, Ls  $121^\circ$ , which  
 273 are randomly divided into a training dataset (1300 MDGMs), a validation dataset  
 274 (586 MDGMs) and a testing dataset (600 MDGMs) and analyze the performance  
 275 in all seasons. Figure 5 and Figure 6 show examples from all four seasons at Ls  
 276  $53.47^\circ$ , Ls  $105.36^\circ$ , Ls  $238.51^\circ$  and Ls  $313.57^\circ$  in MY 26 and MY 27, respectively.  
 277 Figure 5(a-b) and Figure 5(c-d) show detected dust storms at Ls  $53.47^\circ$  (spring) and  
 278 Ls  $105.36^\circ$  (summer). Figure 6(a-b) and Figure 6(c-d) present results at Ls  $238.51^\circ$   
 279 (fall) and Ls  $313.57^\circ$  (winter). Here, our method successfully identifies most of the  
 280 dust storm instances. In the case of slightly overlapping ground-truth objects, at  
 281 least one of both is successfully detected. Also, the center coordinates of some of  
 282 them are mismatched. This may be because the ground-truth rectangles are set by  
 283 visual inspection. Thus, they are to a certain extent subjective and the dust storm  
 284 instances may even extend over a larger area. If so, our method may have identi-  
 285 fied nearby regions because they have similar spatial and spectral characteristics.  
 286 Among others, our method may also have produced some false-negative and false-  
 287 positive cases due to the presence of water ice clouds and/or increased atmospheric  
 288 background dustiness in MDGMs or MDGMs have image gaps, as in Figure 5(d)  
 289 and Figure 6(b) respectively. In line with that, we may integrate some additional  
 290 processes in the future (e.g., filling missing data, cloud detection, etc.).

#### 291 5.4 Distribution of longitude-latitude coordinates

292 Figure 7 (a-d) show the distribution of longitude-latitude coordinates of the pre-  
 293 dicted RoI compared to the subjective coordinates of the ground-truth PRN RoI  
 294 (delta-longitude  $dx$  and delta-latitude  $dy$ ) using the first and the second training  
 295 strategies. We note  $dx$  and  $dy$  are approximately between -4 and 4 of both strategies,  
 296 but longitude variations is more compared to latitude variations, as it is obvious in  
 297 Figures 3, 4, 5 and 6. This is because dust storm events have higher probabilities  
 298 to include a wider area than subjective ground-truth areas.

#### 299 5.5 Comparison with state-of-the-art methods

300 We compare the performance of the regional networks based on the first training  
 301 strategy because it is more significant to predict future dust storms. In Table 1, we  
 302 compare between fast R-CNN, mask R-CNN, SPPnet and the current R-CNN. We  
 303 use mAP with IoU thresholds equal to 25%, 50% and 75%. As expected, selecting  
 304 higher thresholds reduces the effectiveness of all R-CNNs. In addition, inference  
 305 time which is required for each image of all networks between 300-370 milliseconds  
 306 (ms). Mask R-CNNs have higher mAP and faster compared to non-mask networks.  
 307 However, the current method has a slightly higher score because the mask network  
 308 has an additional component ( $Masker_B$ ) that focuses on edges or boundaries to  
 309 refine the mask with minor improvement.

Table 1: Comparison between R-CNNs based on various  $mAP$ .

Method	$mAP_{25}$	$mAP_{50}$	$mAP_{75}$	Time (ms)
Fast R-CNN	64.1	59.1	32.2	350
Mask R-CNN	67.8	61.2	38.1	<b>300</b>
SPPnet	62.5	50.1	22.5	370
Method	<b>68.2</b>	<b>62.1</b>	<b>39.0</b>	320

## 6 Conclusion and outlook

We use mask R-CNN for the automated localization of dust storms in Mars Daily Global Maps (MDGMs) from MGS/MOC. We evaluate the performance of the network by calculating the area under the ROC curves from the dust storm probability images by using various IoU thresholds and obtain the best performance at  $AP_{25}$ . One of the main strengths of this method is its speed and ease of use after training. Potential challenges are due to MDGMs from MGS/MOC partly having gaps (block areas), the R-CNN fails to detect dust storms around these areas. Moreover, it is possible that R-CNN confuses between dust storms and enhanced atmospheric background dustiness in the dust storm season, different dust storms that are near to each other, and/or dust storms and water ice clouds.

The proposed mask R-CNN has been applied to a several-Martian-Year record of satellite images and demonstrated to provide reasonable results at various seasons. We may refine the current results further and thus obtain more accurate dust storm characteristics (location, size, shape, texture, etc.) as follows. It is widely known that Mars dust storms are bright in the red band and dark in the blue band. By contrast, Martian clouds are bright in the red and blue bands and much brighter than the surface in the blue band (Gic19). In the future, we aim to include surface albedo and/or cloudiness when preparing the ground-truth to avoid confusion between dust storms, clouds, and albedo features. Also, we aim to predict the probability of accurate contours based on polygon areas in the MDAD dataset. In addition, we aim to classify each dust storm based on class (main, continuous, sequential, etc.), type (flushing, turning, GDE, etc.) and K16 class (A, C, GDE, etc.). All in all, our method is basically suitable to create another perspective on the climatology of Martian dust storms by a deep-learning-based method.

We attempted to apply the proposed R-CNN on the Mars Reconnaissance Orbiter (MRO) Mars Color Imager (MARCI) from MY 28, Ls 133° (2006) to MY 32, Ls 171° (2014). However, we do not succeed so far. A potential limiting factor is that adjacent global map swath images typically do not overlap and have gaps in between. Apart from that, MDGMs from MRO/MARCI are available as RGBs which consist of red, green and blue components whereas the original MRO/MARCI images consist of seven bands, i.e., five visible bands and two ultraviolet bands. As an outlook for the future, we also consider using feature reduction techniques to define the most significant bands for dust storm detection in case of observations with multiple spectral bands. By implication, our method is particularly interesting for upcoming/future Mars satellite missions/instruments that provide imagery without inherent gaps.

### 347 Abbreviations

348 MDAD: Mars Dust Activity Database; MDGMs: Mars Daily Global Maps; MCS: Mars Climate Sounder; MRO: Mars  
 349 Reconnaissance Orbiter; THEMIS: Thermal Emission Imaging System; MO: Mars Odyssey; TES: Thermal Emission

350 Spectrometer; MGS: Mars Global Surveyor; MOC: Mars Orbiter Camera; MARCI: Mars Color Imager; MCD: Mars  
 351 Climate Database; MY: Martian Year; GDEs: Global Dust Storm Events; EDL: Entry Descent Landing; R-CNN:  
 352 Regional Convolutional Neural Network; PRN: Regional Proposal Network; PCA: Principal Component Analysis;  
 353 MLP: Multi Layer Perceptron; SVM: Support Vector Machine; MAE: Mean Absolute Error; IoU:  
 354 Intersection-over-Union; mAP: mean Average Precision

#### 355 Availability of data and materials

356 The dataset supporting this article is available in the  
 357 <https://dataverse.harvard.edu/dataset.xhtml?persistentId=doi:10.7910/DVN/F8R2JX>.

#### 358 Competing interests

359 The authors declare that they have no competing interest.

#### 360 Funding

361 This work was supported by the New York University Abu Dhabi Institute Grant (ADH01-73-71210-G1502-ADHPG)  
 362 and Emirati Research Grant (ADH01-76-71202-EMIRP-ADHPG).

#### 363 Authors' contributions

364 RA proposed the idea, downloaded all global images, trained the R-CNN and evaluated its performance on Martian  
 365 global images. CG collaborated with the corresponding author in the construction of manuscript. All authors read  
 366 and approved the final manuscript.

#### 367 Acknowledgements

368 The authors acknowledge effort devoted to develop open-source python packages. The authors acknowledge support  
 369 from the New York University Abu Dhabi, Emirati Research Program.

#### 370 Author details

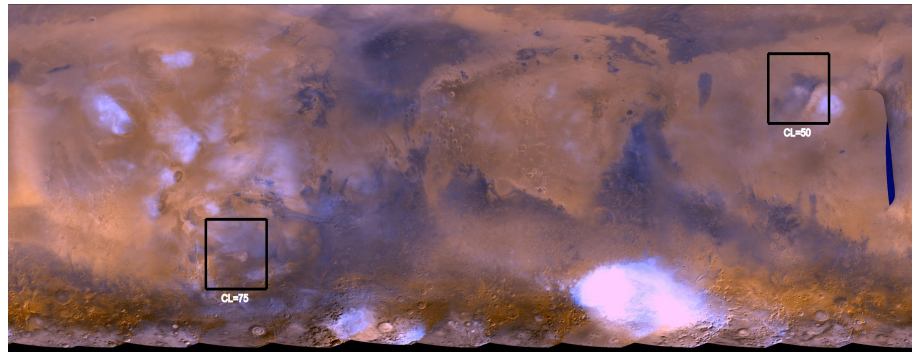
371 <sup>1</sup>Center for Space Science, New York University, Abu Dhabi United Arab Emirate. <sup>2</sup>National Space Science and  
 372 Technology Center, United Arab Emirates University, Al Ain United Arab Emirates.

#### 373 References

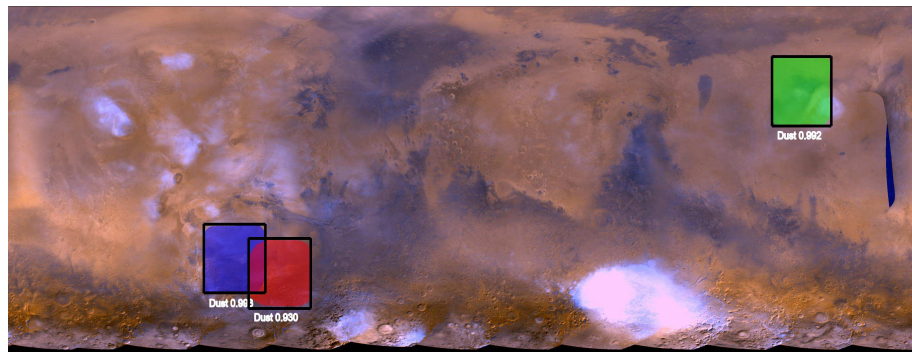
- 374 Bat21. Battalio, M, Wang, H (2021) The Mars Dust Activity Database (MDAD): a comprehensive statistical study  
 375 of dust storm sequences. *Icarus* 354, 114059. doi:10.1016/j.icarus.2020.114059
- 376 Can01. Cantor, B.A, James, P.B, Caplinger, M, Wolff, M.J (2001) Martian dust storms: 1999 mars orbiter camera  
 377 observations. *Journal of Geophysical Research: Planets* 106(E10), 23653–23687. doi:10.1029/2000JE001310
- 378 Can07. Cantor, B.A (2007) MOC observations of the 2001 mars planet-encircling dust storm. *Icarus* 186(1), 60–96.  
 379 doi:10.1016/j.icarus.2006.08.019
- 380 Can19. Cantor, B.A, Pickett, N.B, Malin, M.C, Lee, S.W, Wolff, M.J, Caplinger, M.A (2019) Martian dust storm  
 381 activity near the mars 2020 candidate landing sites: Mro-marci observations from mars years 28–34. *Icarus* 321,  
 382 161–170. doi:10.1016/j.icarus.2018.10.005
- 383 Che20. Cheng, T, Wang, X, Huang, L, Liu, W (2020) Boundary-preserving mask R-CNN. In: *European Conference*  
 384 *on Computer*, pp 660–676
- 385 For17. Forget, F, Montabone, L (2017) Atmospheric dust on Mars: a review. In: *International Conference on*  
 386 *Environmental Systems*
- 387 Geb20. Gebhardt, C, Abuelgasim, A, Fonseca, R.M, Martín-Torres, J, Zorzano, M-P (2020) Fully interactive and  
 388 refined resolution simulations of the martian dust cycle by the marswrf model. *Journal of Geophysical Research:*  
 389 *Planets* 125(9), 2019–006253. doi:10.1029/2019JE006253
- 390 Gic19. Gichu, R, Ogohara, K (2019) Segmentation of dust storm areas on mars images using principal component  
 391 analysis and neural network. *Progress in Earth and Planetary Science* 6(12). doi:10.1186/s40645-019-0266-1
- 392 Gir13. Girshick, R.B, Donahue, J, Darrell, T, Malik, J (2013) Rich feature hierarchies for accurate object detection  
 393 and semantic segmentation. In: *IEEE Conference on Computer Vision and Pattern Recognition*
- 394 Gir15. Girshick, R (2015) Fast R-CNN. In: *IEEE International Conference on Computer Vision*, pp 1440–1448
- 395 Guz15. Guzewich, S.D, Toigo, A.D, Kulowski, L, Wang, H (2015) Mars orbiter camera climatology of textured dust  
 396 storms. *Icarus* 258, 1–13. doi:10.1016/j.icarus.2015.06.023
- 397 Hab17. Haberle, R, Clancy, R, Forget, F, Smith, M, Zurek, R (2017) *The Atmosphere and Climate of Mars*.  
 398 *Cambridge Planetary Science*. Cambridge University Press, Cambridge. doi:10.1017/9781139060172
- 399 He16. He, K, Zhang, X, Ren, S, Sun, J (2016) Deep residual learning for image recognition. In: *IEEE Conference*  
 400 *on Computer Vision and Pattern Recognition*, pp 770–778
- 401 He17. He, K, Gkioxari, G, Dollár, P, Girshick, R (2017) Mask R-CNN. In: *IEEE International Conference on*  
 402 *Computer Vision*, pp 2980–2988
- 403 Hin12. Hinson, D.P, Wang, H, Smith, M.D (2012) A multi-year survey of dynamics near the surface in the northern  
 404 hemisphere of mars: short-period baroclinic waves and dust storms. *Icarus* 219(1), 307–320.  
 405 doi:10.1016/j.icarus.2012.03.001
- 406 Kas16. Kass, D.M, Kleinböhl, A, McCreese, D.J, Schofield, J.T, Smith, M.D (2016) Interannual similarity in the  
 407 martian atmosphere during the dust storm season. *Geophysical Research Letters* 43(12), 6111–6118.  
 408 doi:10.1002/2016GL068978
- 409 Kul17. Kulowski, L, Wang, H, Toigo, A.D (2017) The seasonal and spatial distribution of textured dust storms  
 410 observed by Mars global surveyor Mars orbiter camera. *Advances in Space Research* 59(2), 715–721
- 411 Lin17. Lin, T-Y, Dollár, P, Girshick, R, He, K, Hariharan, B, Belongie, S (2017) Feature pyramid networks for  
 412 object detection. In: *IEEE Conference on Computer Vision and Pattern Recognition*, pp 936–944
- 413 Mae15. Maeda, K, Ogawa, T, Haseyama, M (2015) Automatic martian dust storm detection from multiple  
 414 wavelength data based on decision level fusion. *IPSJ Transactions on Computer Vision and Applications* 7,  
 415 79–83

- 416 Mal10. Malin, M.C, Edgett, K.S, Cantor, B.A, Caplinger, M.A, Danielson, G.E, Jensen, E.H, Ravine, M.A,  
417 Sandoval, J.L, Supulver, K.D (2010) An overview of the 1985-2006 Mars orbiter camera science investigation.  
418 International Journal of Mars Science and Exploration 4, 1–60. doi:10.1555/mars.2010.0001
- 419 Mil16. Milletari, F, Navab, N, Ahmadi, S-A (2016) V-net: fully convolutional neural networks for volumetric  
420 medical image segmentation. In: International Conference on 3D Vision (3DV), pp 565–571
- 421 Mon15. Montabone, L, Forget, F, Millour, E, Wilson, R.J, Lewis, S.R, Cantor, B, Kass, D, Kleinböhl, A, Lemmon,  
422 M.T, Smith, M.D, Wolff, M.J (2015) Eight-year climatology of dust optical depth on Mars. Icarus 251, 65–95.  
423 doi:10.1016/j.icarus.2014.12.034
- 424 New15. Newman, C.E, Richardson, M.I (2015) The impact of surface dust source exhaustion on the Martian dust  
425 cycle, dust storms and interannual variability, as simulated by the marswrf general circulation model. Icarus 257,  
426 47–87. doi:10.1016/j.icarus.2015.03.030
- 427 Ren15. Ren, S, He, K, Girshick, R, Sun, J (2015) Faster r-cnn: Towards real-time object detection with region  
428 proposal networks. In: Advances in Neural Information Processing Systems, vol 28
- 429 Ren16. Ren, S, He, K, Girshick, R, Sun, J (2016) Faster R-CNN: towards real-time object detection with region  
430 proposal networks
- 431 Sim14. Simonyan, K, Zisserman, A (2014) Very deep convolutional networks for large-scale image recognition. In:  
432 International Conference on Learning Representations
- 433 Wan02. Wang, H, Ingersoll, A.P (2002) Martian clouds observed by Mars global surveyor Mars orbiter camera.  
434 Journal of Geophysical Research: Planets 107(E10), 8–1816. doi:10.1029/2001JE001815
- 435 Wan15. Wang, H, Richardson, M.I (2015) The origin, evolution, and trajectory of large dust storms on Mars during  
436 Mars years 24–30 (1999–2011). Icarus 251, 112–127. doi:10.1016/j.icarus.2013.10.033
- 437 Zur93. Zurek, R.W, Martin, L.J (1993) Interannual variability of planet-encircling dust storms on Mars. Journal of  
438 Geophysical Research: Planets 98(E2), 3247–3259. doi:10.1029/92JE02936

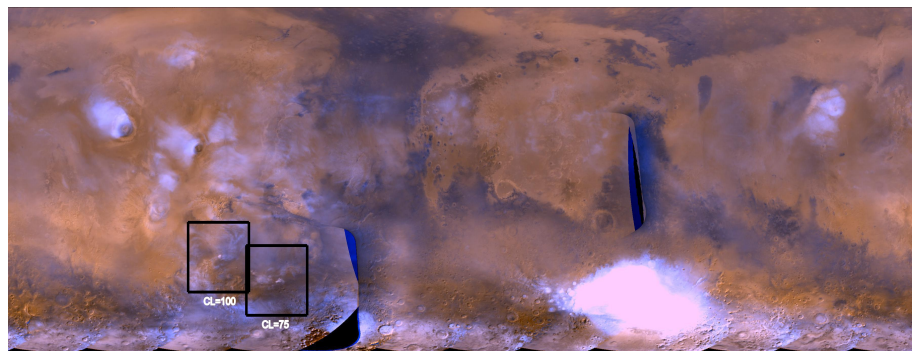
Figure 3: 1<sup>st</sup> strategy: the training and validation images are selected randomly from MY 25 to middle of MY 27. The testing images are selected randomly from middle of MY 27 to MY 28. (a) and (c) are ground-truth images from spring and summer seasons and (b) and (d) are their predicted dust maps.



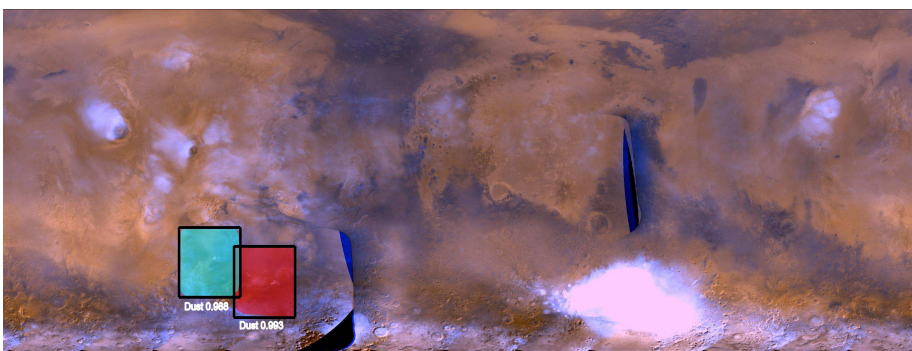
(a)



(b)

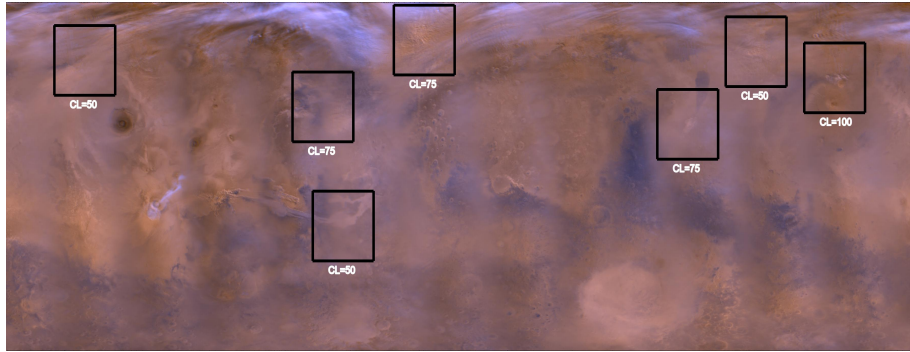


(c)

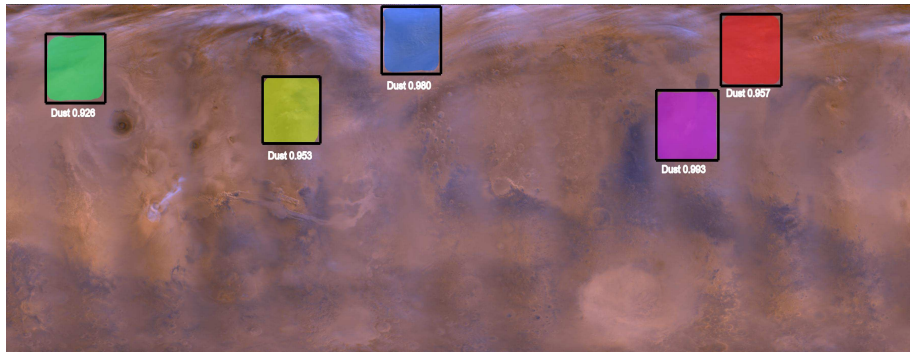


(d)

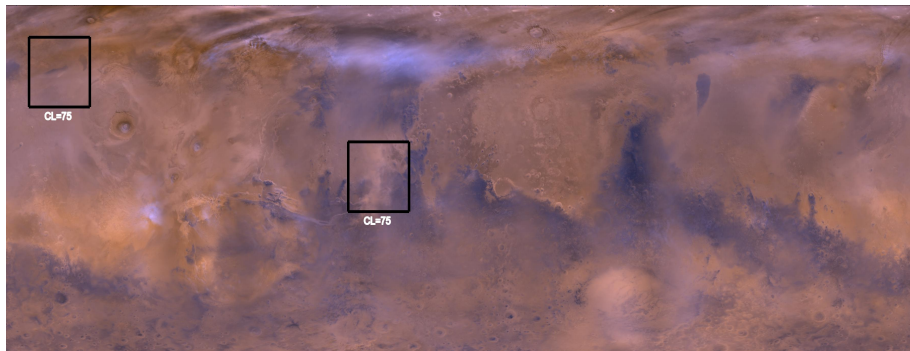
Figure 4: 1<sup>st</sup> strategy: the training and validation images are selected randomly from MY 25 to middle of MY 27. The testing images are selected randomly from middle of MY 27 to MY 28. (a) and (c) are ground-truth images from fall and winter seasons and (b) and (d) are their predicted dust maps.



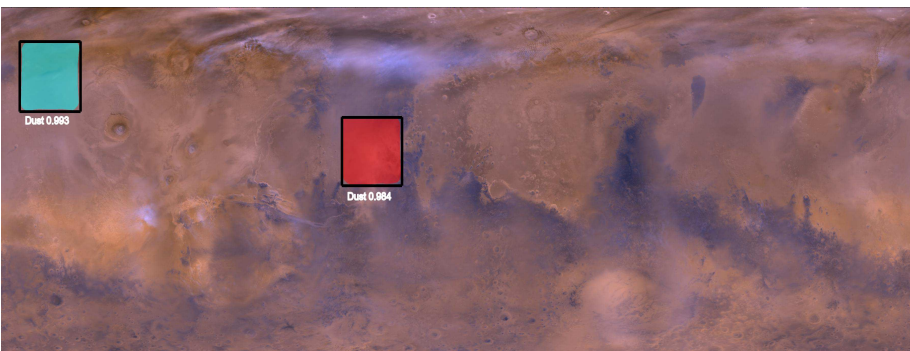
(a)



(b)

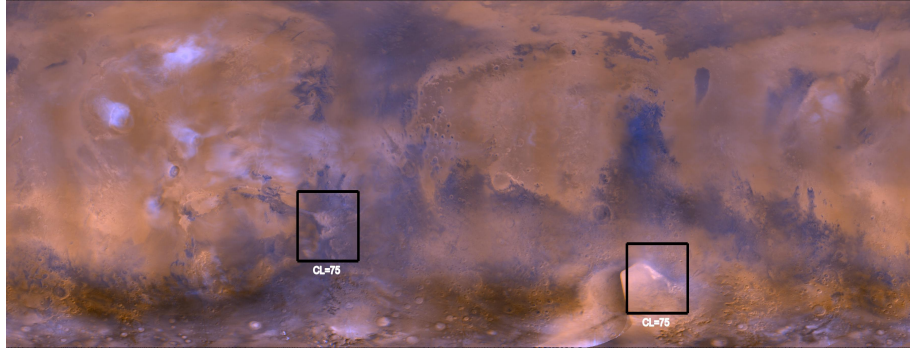


(c)

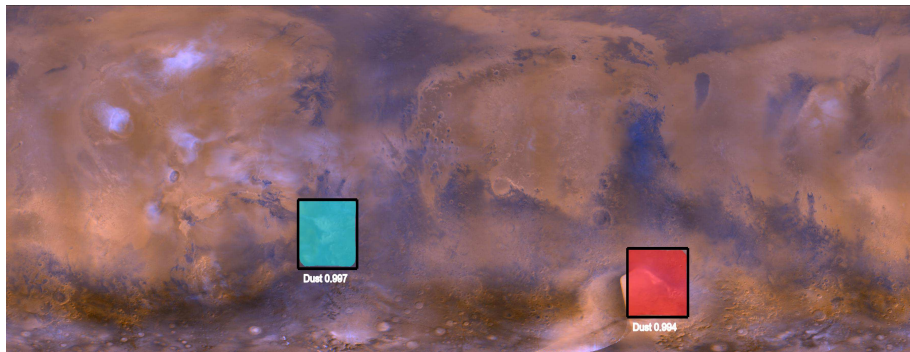


(d)

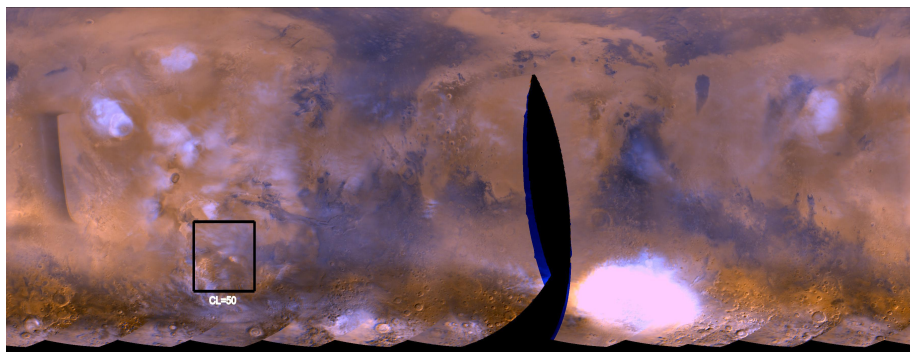
Figure 5: 2<sup>nd</sup> strategy: the training, validation and testing images are selected randomly from MY 25 to MY 28. (a) and (c) are ground-truth images from spring and summer seasons and (b) and (d) are their predicted dust maps.



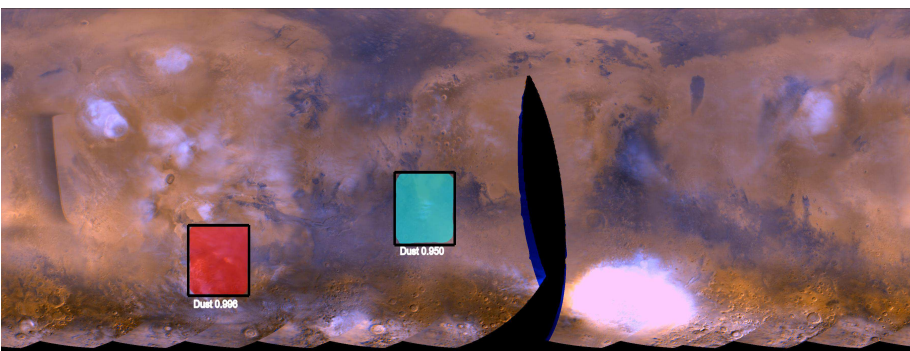
(a)



(b)

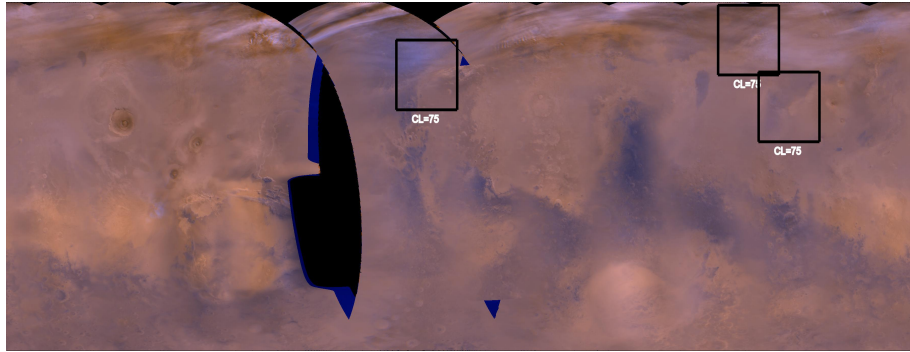


(c)

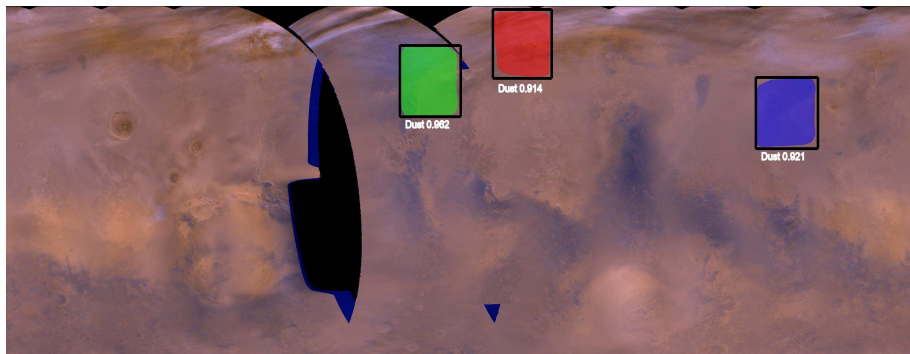


(d)

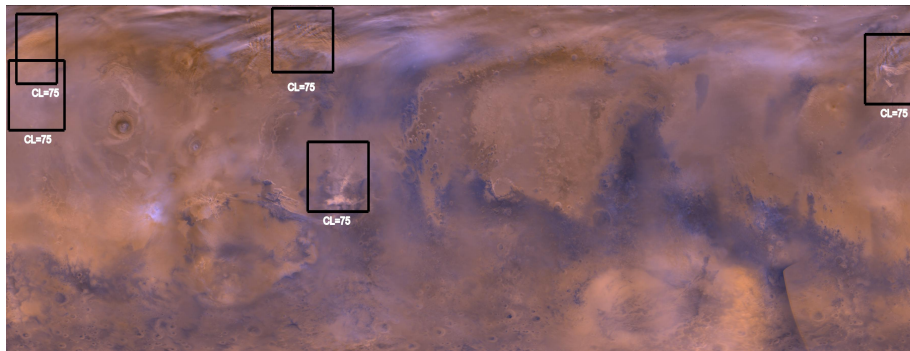
Figure 6: 2<sup>nd</sup> strategy: the training, validation and testing images are selected randomly from MY 25 to MY 28. Left panel shows ground-truth maps and right panel shows predicted maps. (a) and (c) are ground-truth images from fall and winter seasons and (b) and (d) are their predicted dust maps.



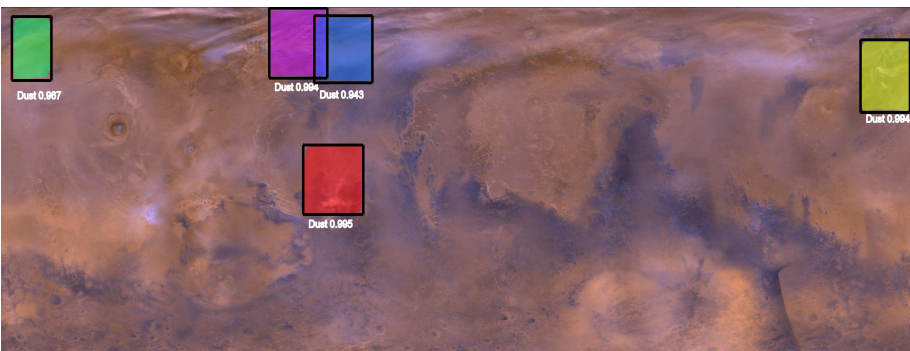
(a)



(b)



(c)



(d)

